

Joussame

CNRS - Université Pierre et Marie Curie - Université Versailles-Saint-Quentin  
CEA - ORSTOM - Ecole Normale Supérieure - Ecole Polytechnique

# Institut Pierre Simon Laplace

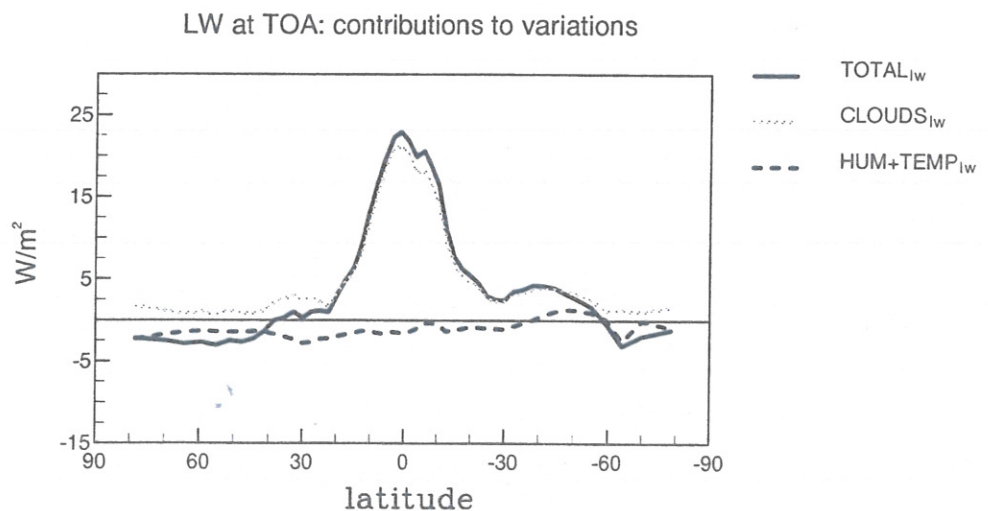
des Sciences de l'Environnement Global

## *Notes du Pôle de Modélisation*

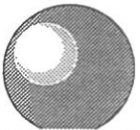
Long term climate drift of a coupled surface  
ocean-atmosphere model : role of ocean heat  
transport and cloud radiative feedbacks

Emmanuelle Cohen-Solal and Hervé Le Treut

Laboratoire de Météorologie Dynamique du CNRS





 I P S L	<b>CNRS - Université Pierre et Marie Curie - Université Versailles-Saint-Quentin</b> <b>CEA - CNES - ORSTOM - Ecole Normale Supérieure - Ecole Polytechnique</b>	
	<b>Institut Pierre Simon Laplace</b> <b>des Sciences de l'Environnement Global</b>	
	<b>CETP - LMD - LODYC - LPCM - LSCE - SA</b>	
	<table border="0"> <tr> <td data-bbox="190 465 847 582"> <b>Université Pierre-et-Marie-Curie</b>            B 102 - T15-E5 - 4, Place Jussieu            75252 Paris Cedex 05 (France)            Tél : (33) 01 44 27 39 83            Fax : (33) 01 44 27 37 76         </td> <td data-bbox="847 465 1296 582"> <b>Université Versailles-Saint-Quentin</b>            Collège Vauban, 47 Boulevard Vauban            78047 Guyancourt Cedex (France)            Tél : (33) 01 39 25 58 17            Fax : (33) 01 39 25 58 22         </td> </tr> </table>	<b>Université Pierre-et-Marie-Curie</b> B 102 - T15-E5 - 4, Place Jussieu 75252 Paris Cedex 05 (France) Tél : (33) 01 44 27 39 83 Fax : (33) 01 44 27 37 76
<b>Université Pierre-et-Marie-Curie</b> B 102 - T15-E5 - 4, Place Jussieu 75252 Paris Cedex 05 (France) Tél : (33) 01 44 27 39 83 Fax : (33) 01 44 27 37 76	<b>Université Versailles-Saint-Quentin</b> Collège Vauban, 47 Boulevard Vauban 78047 Guyancourt Cedex (France) Tél : (33) 01 39 25 58 17 Fax : (33) 01 39 25 58 22	

# Long term climate drift of a coupled surface ocean-atmosphere model : role of ocean heat transport and cloud radiative feedbacks

Emmanuelle Cohen-Solal and Hervé Le Treut

Laboratoire de Météorologie Dynamique du CNRS

Nous décrivons le biais initial du climat simulé par un modèle couplé océan-atmosphère. La composante atmosphérique du modèle est le modèle de circulation générale du Laboratoire de Météorologie Dynamique. La composante océanique est limitée à l'océan de surface mais incorpore une couche mélangée dont l'épaisseur est calculée par le modèle. Comme la circulation générale de l'océan n'est pas décrite par le modèle, on prescrit le transport horizontal de chaleur à l'intérieur de l'océan. Le biais initial du modèle est modifié par des changements introduits dans ce terme prescrit de transport de la chaleur dans l'océan. Nous analysons ici une expérience dans laquelle cette dérive est particulièrement forte. Nous cherchons notamment à mettre en évidence les processus fondamentaux qui relient les changements du transport océanique de chaleur et l'évolution temporelle du climat modélisé. Dans cette simulation, la température océanique se refroidit de l'ordre de 1.5C en 20 ans. Deux périodes peuvent être distinguées. Pendant la première période, longue de 5 ans, la température de surface de l'océan se refroidit, particulièrement dans les tropiques mais les pertes par rayonnement infrarouge au sommet de l'atmosphère augmentent rapidement, notamment à la fin de la période.

<b>Mai 1998</b> <b>Note n° 6</b>
-------------------------------------





Une version diagnostique "off-line" du code radiatif du modèle d'atmosphère nous permet de décomposer ce comportement en différentes contributions (nébulosité, humidité spécifique, températures de la surface et de l'air, albédo de surface). Cette partition montre que l'évolution du flux infrarouge au sommet de l'atmosphère est due à la diminution des nuages hauts (cirrus) de la troposphère de la région intertropicale. La diminution de ces nuages entraîne également une diminution de l'albédo planétaire et par conséquent, une augmentation du rayonnement solaire absorbé par le système climatique. Mais la contribution dominante est le refroidissement par le rayonnement infrarouge qui destabilise le système et l'écarte de son équilibre. Pendant le reste de la simulation (deuxième période), le refroidissement lié à la destabilisation au sommet de l'atmosphère est transmise à la surface par les divers processus en jeu dans le système climatique.

Ainsi, nous montrons que de petites variations du transport océanique de chaleur peut conduire le modèle d'un état stable à un état instable au travers de processus atmosphériques qui se mettent en route lorsque les tropiques se refroidissent. Bien que probablement surestimé par notre modèle, le mécanisme mis en évidence peut être déterminant pour le climat réel dans les tropiques et les simplifications propres à la structure de notre modèle nous permettent de l'étudier en détail.



**Long term climate drift of a coupled surface ocean-atmosphere  
model: role of ocean heat transport and cloud radiative feedbacks.**

Emmanuelle Cohen-Solal and Hervé Le Treut

Laboratoire de Météorologie Dynamique du CNRS, Université Pierre et Marie Curie, Tour 25-15, 5ème étage, Case courrier 99, 4 place Jussieu, 75252 Paris cedex 05, FRANCE. Tel: 33-1-44 27 47 72, Fax: 33-1-44 27 62 72.

Submitted to Climate Dynamics.

## Abstract

We describe the initial bias of the climate simulated by a coupled ocean-atmosphere model. The atmospheric component is a state-of-the-art atmospheric general circulation model, whereas the ocean component is limited to the upper ocean and includes a mixed layer whose depth is computed by the model. As the full ocean general circulation is not computed by the model, the heat transport within the ocean is prescribed. When modifying the prescribed heat transport we also affect the initial drift of the model. We analyze here one of the experiments where this drift is very strong, in order to study the key processes relating the changes in the ocean transport and the evolution of the model's climate. In this simulation, the ocean surface temperature cools by  $1.5^{\circ}\text{C}$  in 20 years. We can distinguish two different phases. During a first period of 5 years, the sea surface temperatures become cooler, particularly in the intertropical area, but the outgoing longwave radiation at the top of the atmosphere increases very quickly, in particular at the end of the period. An off-line version of the model radiative code enables us to decompose this behaviour into different contributions (cloudiness, specific humidity, air and surface temperatures, surface albedo). This partitioning shows that the longwave radiation evolution is due to a decrease of high level cirrus clouds in the intertropical troposphere. The decrease of the cloud cover also leads to a decrease of the planetary albedo and therefore an increase of the net short wave radiation absorbed by the system. But the dominant factor is the strong destabilization by the longwave cooling, which is able to throw the system out of equilibrium. During the remaining of the simulation (second phase), the cooling induced by the destabilization at the top of the atmosphere is transmitted to the surface by various processes of the climate system.

Hence, we show that small variations of ocean heat transport can bring the model from a stable to an unstable state via atmospheric processes which arise when the tropics are cooling. Even if possibly overestimated by our GCM, this mechanism may be pertinent to the maintenance of present climatic conditions in the tropics. The simplifications inherent in our model's design allow us to investigate the mechanism in some detail.

## 1 Introduction

All climate change experiments involving coupled ocean/atmosphere models are faced with the problem of simulating a control climate corresponding to present climate conditions. In uncoupled simulations, fixed boundary conditions at the ocean-atmosphere interface act as relaxation terms. When atmosphere and ocean models are coupled together without further adjustment, however, these relaxation constraints are typically absent and the resulting coupled model has much more freedom to evolve than each uncoupled component. Without some form

of flux correction (Sausen et al. 1988), the coupled simulation will therefore frequently drift gradually into an equilibrium state which can be far from present-day climate conditions (Braconnot et al. 1997; Hasselmann 1988; Rahmstorf 1995; Weaver and Hughes 1996; for an exception see Boville et al. 1997). In this new state both the atmosphere and the ocean are different from their uncoupled states. If the simulated climate is very unrealistic, the usefulness of the coupled model for sensitivity experiments may be compromised.

A relevant problem is therefore the stability of the unforced climate system both in reality and as simulated by numerical models. This problem is important for two reasons: potential instabilities of coupled models affect our capacity to carry out realistic numerical simulations, and the processes involved in the model instabilities may also be partly responsible for the natural variability of the climate system.

In this paper we study a version of the LMD (Laboratoire de Météorologie Dynamique, Paris, France) atmospheric general circulation model (AGCM) coupled to a simplified ocean model in which spontaneous instabilities occur depending on parameters such as the prescribed ocean horizontal transport of energy. We show here that small variations of the ocean heat transport can shift the model from a stable state into an unstable one via atmospheric radiative mechanisms which operate when there is a surface cooling of the tropical oceans. Our experiments constitute an attempt to study those instabilities in a rather simplified framework, where the coupling with the ocean is limited to its thermodynamic component. It is useful to remember, though, that surface instabilities in the model can be larger than in reality or in other models because the horizontal temperature mixing by the ocean dynamics is not physically represented and instabilities can develop locally.

Section 2 gives a short description of the model. The temporal evolution of the coupled model's climate is described in section 3. In section 4.1, we present a method for partitioning the evolution of the radiative fluxes into contributions due to clouds, temperature, specific humidity and surface albedo, using an off-line version of the model radiative code. The results are shown in section 4.2. A discussion and conclusions are presented in section 5.

## 2 The model

### 2.1 Description

The coupled model studied here has been described in detail in Cohen-Solal and Le Treut (1996, 1997). We summarize here its main characteristics only.

The atmosphere is represented by the atmospheric general circulation model developed at the Laboratoire de Météorologie Dynamique (Sadourny and Laval, 1984) in its cycle 4 version (Le Treut and Li 1991). It is a grid point model



with points equally spaced in sine of latitude and in longitude, and irregularly spaced on the vertical. In the chosen resolution, there are 64 longitudinal points, 50 latitudinal points and 11 sigma levels in the atmosphere. The horizontal resolution in longitude  $\times$  latitude is about  $5.6^\circ \times 2.3^\circ$  at the equator and  $5.6^\circ \times 3.5^\circ$  in mid-latitudes. The short wave radiation scheme is adapted from Fouquart and Bonnel (1980) and the longwave radiation scheme is due to Morcrette (1991). These schemes are also used in the operational model of the European Centre for Medium range Weather Forecasts (but Morcrette's scheme has undergone changes in some parameters for water vapor's absorption). There is no diurnal cycle in this version of the AGCM, but it includes a seasonal cycle of insolation.

The cloud formation is prognostically determined as described in Le Treut and Li (1991). Time dependent cloud liquid water content is predicted by a conservation equation involving rates of water vapor condensation, evaporation of cloud droplets and the transformation of cloud droplets in precipitating drops. The cloud liquid water content also determines cloud cover and cloud optical properties. The cloud cover is the greater of the fraction of convective cloud and the fraction of stratiform cloud. The fraction of convective cloud in a grid box is unity if moist convective adjustment is invoked; otherwise, it is given by the surface fraction of the active cumulus cloud obtained from the Kuo (1965) scheme. Cloud forms in those layers where there is a decrease in water vapor from one call of the convective scheme to the next (every 30 minutes), and the cloud liquid water content is redistributed in these layers proportional to this decrease. The fraction of stratiform clouds is determined from the probability that the total cloud water (liquid plus vapor) is above the saturated value. (A uniform probability distribution is assumed with a prescribed standard deviation.) This stochastic approach also crudely simulates the effects of evaporation of cloud droplets. The effect of clouds on radiation involves the cloud liquid water content distribution on the atmospheric column. Clouds are considered to overlap randomly. There exist only two kinds of droplets depending on the phase (liquid or ice) of the water in the cloud. The phase is determined by the temperature of the top of the cloud.

At the surface, evaporation and sensible heat flux are expressed by bulk formulae in which the drag coefficient is crudely expressed as only dependent on the season and the type of surface (rougher over land and sea ice and in winter). The land has only one layer for the determination of ground temperature and soil moisture and does not include an explicit scheme for the biosphere. Over land and sea ice, the turbulent heat fluxes are part of the implicit scheme of the planetary boundary layer determination.

The ocean component has the same horizontal representation as the atmosphere. There are 20 vertical levels unevenly distributed over the 800 metres of the ocean. The surface layer is a perfectly mixed layer. Its depth, ranging from 15 m to a maximum of 800 m, is determined according to Gaspar (1988). It depends on the wind stress at the surface of the ocean, heat fluxes exchanged

with the atmosphere, and the internal density distribution. In this version of the model, the effects of precipitation and evaporation on the mixed layer scheme are neglected, but the fresh water/salt flux due to sea ice variations is taken into account. The heat fluxes exchanged with the atmosphere are applied throughout the mixed layer except for a small part of the short wave radiation which can penetrate deeper (Cohen-Solal and Le Treut 1996). The ocean has a flat bottom at a depth of 800 meters with no exchange of fluxes.

The sea ice model is thermodynamical only. The presence of open water, which in the real world results from mechanical deformation of sea ice, is parameterized according to Hibler (1979). The thermodynamics of the grid cell fraction covered with ice is represented by a simplified model from Semtner (1976) but without snow cover. The ice freezes and melts as a result of the imbalance between oceanic and atmospheric heat fluxes. The sea ice temperature is interactively calculated within the planetary boundary layer calculation, but ice adjusts instantaneously (no heat capacity). The net heat flux between the atmosphere and the ice balances the heat transmitted by conduction between the bottom and the surface of the ice block. Converted into ice thickness, it gives the rate of melting or accretion as a result of the ice/atmosphere coupling. A decomposition of these fluxes between the grid cell fraction covered with ice and the open water (darker and warmer than the ice surface) gives an estimation of the closure or opening of the latter. At the ice/ocean interface, when ice is present, the ocean is maintained at the freezing point, the heat imbalance being absorbed by the ice.

At the ocean/atmosphere interface, all the fluxes are explicitly determined and are exchanged without flux correction.

## 2.2 Parametrization of the ocean heat transport

Since the large scale ocean circulation is not simulated, the oceanic energy transport must be prescribed. Our method is the following: We first run the uncoupled version of the LMD AGCM constrained by realistic surface boundary conditions of sea surface temperatures and sea ice cover. At each model grid point, we diagnose the ocean heat transport divergence as the mean over the simulation of the surface heat fluxes (called  $F_o$ ): defined in this way, the annual mean ocean heat transport naturally balances the annual mean ocean/atmosphere heat fluxes, when annual averages are computed over a few years. This term (in  $\text{W/m}^2$ ) is constant with time (it is an annual mean) and is applied as a complementary diabatic term in the mixed layer heat budget for the coupled simulations. The northward ocean heat transport (in Watts) is implied by integrating the previous term from one pole to the other over the ocean grid cells.

The whole procedure is described in detail by Cohen-Solal and Le Treut (1997). The authors show that the computed term is within the observational uncertainties. However, these uncertainties are very large (Gleckler and Weare 1997) and the surface heat fluxes computed by atmospheric models are generally

within the error bounds (e.g. Gleckler et al. 1995).

### 2.3 Motivation and experimental design

In addition to the large uncertainties in the observations, the ocean heat transport directly simulated by ocean general circulation models varies dramatically from model to model. This is evident from analysis of the models participating in Coupled Model Intercomparison Project CMIP (Covey et al. 1996). Our motivation here is to study the impact of varying oceanic heat transport, in a simplified model framework on the long term evolution of our coupled model's climate. And, indeed, we have found that small perturbations of the prescribed oceanic heat transport, i.e. less than those implied by the observational error bounds, can trigger atmospheric feedbacks and thus generate substantial drifts in coupled simulations.

Toward this goal, we have computed two other ocean heat transports by modifying the surface heat flux,  $F_o$ , simulated by the uncoupled atmospheric simulation. (In the conventions of this text, a positive value for  $F_o$  corresponds to a divergence for the implied ocean heat transport.) In one case,  $F_o$  was reduced by  $20 \text{ W/m}^2$  between latitudes  $10\text{S}$  and  $10\text{N}$ , and  $5.7 \text{ W/m}^2$  were added outside this area. This is equivalent to lowering the divergence of heat transport at low latitudes and the convergence at higher latitudes: the implied northward ocean heat transport is therefore less active in transporting heat from equator to poles. The second case corresponds to the inverse of the first (same amounts as previously, but with opposite signs), resulting in an implied ocean heat transport which is more active in transporting heat from equator to poles. The values of the perturbations, which are lower than the observational error bounds, have been chosen so that the global mean over the ocean is equal to zero. Therefore, the perturbations of the ocean heat transport do not add or remove heat to the ocean in global mean term.

For all the simulations performed with the LMD model, the atmosphere dynamics time step is 6 minutes, and adiabatic processes are computed every 30 minutes. In coupled simulations, the ocean and sea ice are called every day. The carbon dioxide concentration in the atmosphere is fixed at a value of 320 ppbv (roughly average between preindustrial and present-day concentrations).

Table 1 lists the simulations performed with our model. First, we perform an uncoupled simulation with the LMD AGCM, here denoted as ATMO. This run is also used in Cohen-Solal and Le Treut (1996, 1997) It is realistically forced by climatological sea surface temperatures interpolated horizontally and vertically from the climatology of Levitus (1982) and by sea ice cover taken from Alexander and Mobley (1976). The 8 year mean of the net surface heat flux simulated by ATMO gives the ocean heat transport as described in section 2.2 and Cohen-

Run	Name	Model Version	Ocean heat Transport	length
1)	ATMO	uncoupled AGCM	diagnosed	8 years
2)	STANDARD	coupled model	standard	70 years
3)	TRANSP <sup>+</sup>	coupled model	more divergent	20 years
4)	TRANSP <sup>-</sup>	coupled model	less divergent	20 years

Table 1: List of the simulations: runs **2)** to **4)** are performed with the same coupled model but with different ocean heat transport terms. Run **1)** is performed with the LMD AGCM (Cycle 4) forced by prescribed oceanic boundary conditions. The differences between the versions are indicated in the table. The atmospheric model is identical in each case.

Solal and Le Treut (1997). Runs 2 to 4 consist of coupled simulations of various lengths from 20 to 70 years. The longest simulation, called STANDARD (run 2 in Tab. 1), has already been described in Cohen-Solal and Le Treut (1996, 1997). It is performed with the ocean heat transport diagnosed from ATMO. TRANSP<sup>-</sup> and TRANSP<sup>+</sup> are computed with the modified ocean heat transports. TRANSP<sup>-</sup> is performed with the ocean heat transport term which implies a less active transport of heat from equator to poles; and TRANSP<sup>+</sup>, with the more active transport of heat.

### 3 Long-term evolution of the model climate for different ocean heat transports

#### 3.1 Sea surface temperatures

Fig. 1 shows the behaviour of global mean sea surface temperature for the coupled simulations given in Table. 1. All simulations drift towards a colder state. In STANDARD, after the initial 5 year period where SSTs are stable in the global annual mean, they decrease at a rate of .4°C/decade. In TRANSP<sup>-</sup>, the SSTs first increase and after roughly 5 years decrease at approximately the same rate as STANDARD. In TRANSP<sup>+</sup>, the SSTs become colder with an acceleration of the cooling rate after 5-6 years (approximately equal to 1.°C/decade). Hence, the comparison of the 3 simulations shows that the ocean heat transport perturbations, although equal to zero in global average terms, have substantial impact on the global drift: TRANSP<sup>-</sup> is warmer than STANDARD, and TRANSP<sup>+</sup> is cooler, with a faster drift than STANDARD. We will mainly study TRANSP<sup>+</sup> and compare it to TRANSP<sup>-</sup> when required.

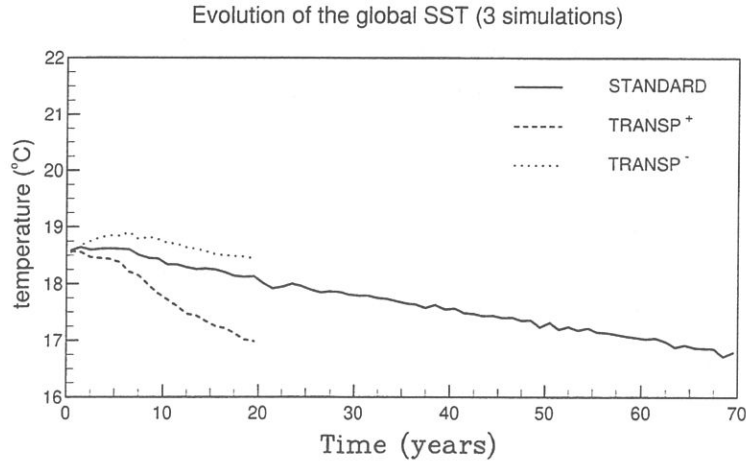


Figure 1: Time evolution (in  $^{\circ}\text{C}$ ) of the global-mean annual-mean sea surface temperature for the three coupled simulations of Table 1. STANDARD is computed with the original ocean heat transport term,  $\text{TRANSP}^+$  with a more active poleward ocean heat transport and  $\text{TRANSP}^-$  with a less active poleward ocean heat transport.

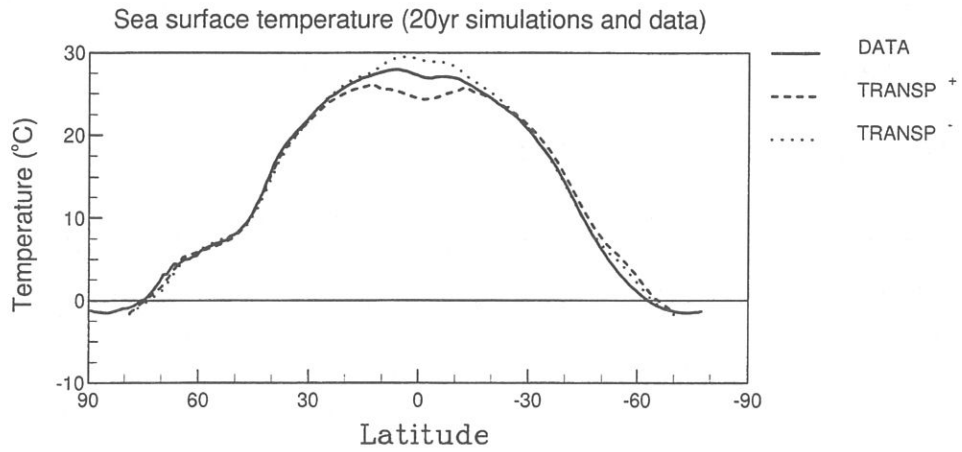


Figure 2: zonal-mean SST (in  $^{\circ}\text{C}$ ) averaged over the 20 years of simulation for  $\text{TRANSP}^+$  (dashed line) and  $\text{TRANSP}^-$  (dotted line). They are compared to observations taken from Levitus (solid curve).



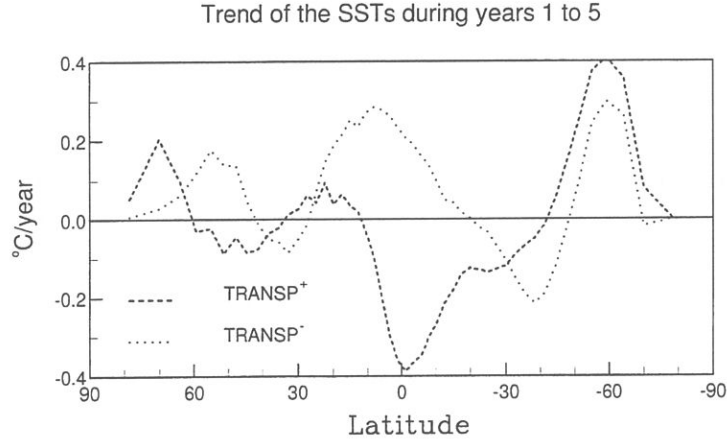


Figure 3: Slope of the least-squares linear trend of the sea surface temperatures (in  $^{\circ}\text{C}/\text{year}$ ) for years 1 to 5 of the coupled simulations  $\text{TRANSP}^+$  and  $\text{TRANSP}^-$ .

### 3.2 Characteristic of the trend

Fig. 2 gives the zonal-mean SSTs simulated in the  $\text{TRANSP}^+$  and  $\text{TRANSP}^-$  integrations. Results are averaged over the 20 years of the simulations. Data from the Levitus climatology (Levitus 1982) are also shown. As a consequence of the intentional perturbations of the ocean heat transport, the SST simulated by  $\text{TRANSP}^+$  is too cold in the intertropical region; the opposite is true for  $\text{TRANSP}^-$ . Outside of this area,  $\text{TRANSP}^+$  is very slightly warmer than  $\text{TRANSP}^-$ . But, on the other hand, both simulations have a warm anomaly in the southern hemisphere regardless of the sign of the heat transport perturbation. More generally, the anomalies are far from being uniform over the globe whereas the perturbations of the ocean heat transport are uniform respectively in the tropical area and outside. Therefore, the differences between the simulations and the observations are not only consequences of the direct effect of ocean heat transport perturbations but also induced feedbacks.

To illustrate the complex temporal characteristics of the sea surface temperature evolution, we compute at each grid-point the slope of the least squares linear trend of the SSTs time series.  $\text{TRANSP}^+$  and  $\text{TRANSP}^-$  SST trends are computed for two periods: years 1 to 5 and years 8 to 20 corresponding to periods before and after the change in the slope of global annual mean SST (Fig. 1).

#### 3.2.1 Years 1-5

The comparison of the curves in Fig. 3 shows that  $\text{TRANSP}^+$  and  $\text{TRANSP}^-$  have different behaviour during the first 5 years. While  $\text{TRANSP}^+$  is cooling in the equatorial area,  $\text{TRANSP}^-$  is warming. This is consistent with the signs of the heat transport anomalies, except that for both simulations the SST response goes

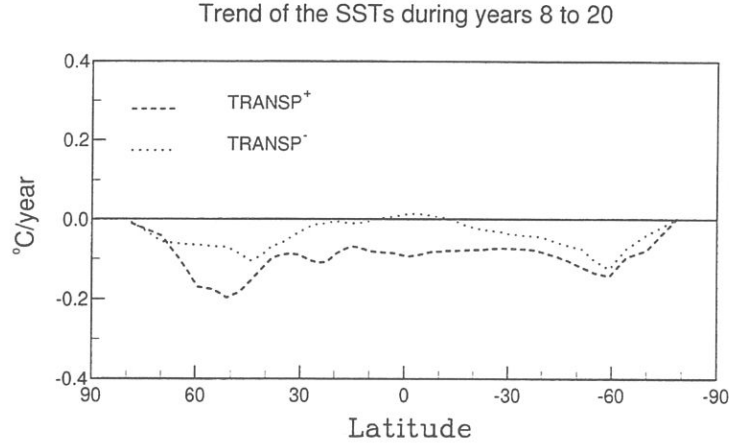


Figure 4: Same as Fig. 3 but for years 8 to 20.

beyond the 10S-10N area where the transport anomalies changed signs. In mid latitudes of the northern hemisphere (about 50N)  $\text{TRANSP}^+$  becomes cooler and  $\text{TRANSP}^-$  warmer: the signs are therefore opposite to those of the heat transport anomalies in this area.

In the southern ocean, the simulations have somewhat similar warming trends. This is due to the melting of sea ice in interaction with the initial ocean heat content: the ocean's first 100 metres initially contain enough heat to melt a 1-meter thick sea ice block covering all locations off-shore of the Antarctic continent. This adjustment does not occur instantaneously because it involves the vertical mixing in the ocean which brings warmer sub-surface water from intermediate and deeper ocean layers to the surface. This multi-year adjustment of the ice-ocean coupling is present in all coupled runs (runs 2 to 4 in Tab. 1).

### 3.2.2 Years 8-20

Whereas the first period showed latitudinally-varying SST adjustment patterns, the second period exhibits a more uniform pattern (Fig. 4). The trends in  $\text{TRANSP}^+$  and  $\text{TRANSP}^-$  are now more similar in sign except for the fact that  $\text{TRANSP}^-$  is slightly positive in the 10S-10N area. Differences in the size of SST trends are apparent:  $\text{TRANSP}^+$  has a stronger cold bias than  $\text{TRANSP}^-$ , even in regions where the anomaly of the ocean heat transport is positive (i.e., outside the 10S-10N band). In the next sections, we analyse the feedbacks which affect the initial response that we find in  $\text{TRANSP}^+$ .

## 3.3 Ocean global heat content

The global heat content of the ocean is indicated by its temperature averaged over latitude, longitude and depth. The time evolution of the spatially averaged

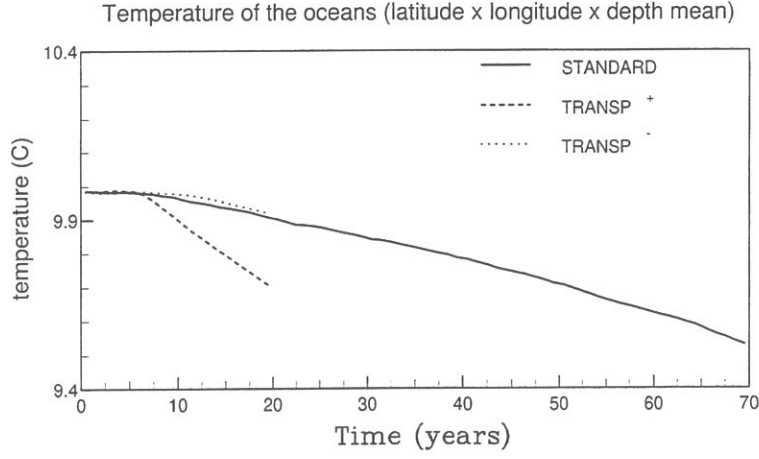


Figure 5: Time evolution (in  $^{\circ}\text{C}$ ) of the annual-mean global-mean temperature of the ocean (horizontally and vertically averaged), for STANDARD,  $\text{TRANSP}^+$  and  $\text{TRANSP}^-$ .

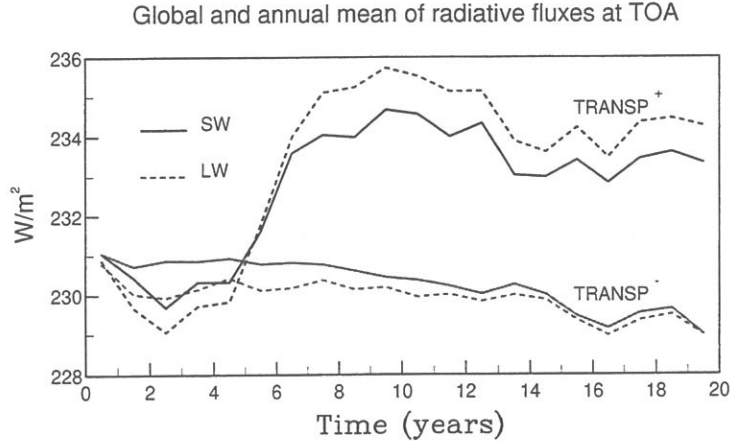


Figure 6: Time evolution (in  $\text{W}/\text{m}^2$ ) of the annual-mean global-mean longwave (LW, dotted curves) and shortwave (SW, plain curves) radiation at the top of the atmosphere for  $\text{TRANSP}^+$  (upper curves) and  $\text{TRANSP}^-$  (lower curves). Outgoing (incoming) LW (SW) is positive in sign.

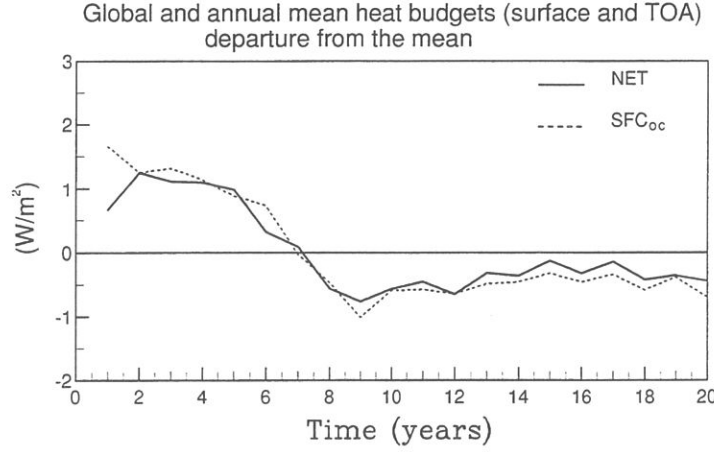


Figure 7: Time evolution in  $\text{TRANSP}^+$  (in  $\text{W/m}^2$ ) of the global annual-mean net radiative budget at the top-of-the-atmosphere (solid curve) and the net surface heat budget over the ocean only (but distributed appropriately over the entire globe; dashed curve). Values represent departures from the respective temporal means.

temperatures for STANDARD,  $\text{TRANSP}^+$  and  $\text{TRANSP}^-$  are shown in Fig. 5. For the first 6 years of the simulations, the ocean heat content is very similar in the 3 simulations. After the 6th year, there is a drastic change in the slope for  $\text{TRANSP}^+$ , which starts to cool at a rate of  $0.2^\circ\text{C}/\text{decade}$ . The slope of the ocean heat content is equal to the heat budget for the ocean (net surface heat flux plus ocean heat transport). The behaviour of  $\text{TRANSP}^+$  indicates that after 6 years of quasi equilibrium in global mean terms, there is a large and rapid loss of heat from the ocean. The key feedbacks that cause this unstable behaviour in  $\text{TRANSP}^+$  are studied below.

### 3.4 Fluxes at the top of the atmosphere

The study of the climate energetics starts with the examination of the radiative fluxes at the top of the atmosphere (TOA). The difference between the net short wave radiation flux (SW hereafter: insolation less reflected radiation) and the outgoing longwave radiation flux (LW) controls the evolution of the global climate system. Fig. 6 gives the temporal evolution of the global-mean annual-mean SW and LW simulated by  $\text{TRANSP}^+$  and  $\text{TRANSP}^-$ . In  $\text{TRANSP}^-$ , the SW and LW slightly decrease and become closer to each other with time: the net radiative budget tends to zero. But note that the (small) value of the net radiative budget at the top of the atmosphere does not give the actual tendency of the system. That is because there are non-conservative processes in the atmospheric model, such as the non-conversion of dissipated kinetic energy, removed from the momentum equations, into heat: such processes generally involve amounts of energy

which are negligible in a forced atmospheric model compared to the solar and sea surface temperature forcings, but which may be significant in coupled models. For this reasons, a "perfect" simulated energy balance is not inconsistent with a non-zero mean radiative budget at the TOA. This is not considered as a problem for this study because we are concerned with differences and not with absolute values of the heat fluxes.

TRANSP<sup>+</sup>, in contrast, shows rapid increases (between years 5 and 7) in the LW and SW fluxes at the TOA. In view of the large surface cooling this LW increase was somewhat unexpected. The increase is greater than 5 W/m<sup>2</sup> in global-mean annual-mean terms. There is simultaneously a SW increase of ca. 3.5 W/m<sup>2</sup>: this does not compensate for the LW increase, and therefore the net radiative budget switches from positive to negative. This decreasing of the net radiative budget at the TOA tends to additionally cool the model.

It is very difficult to analyse how this destabilisation is transmitted to the surface because it involves many different climate processes. Nevertheless, the destabilisation evidence can be seen in the global annual mean of the ocean's temperatures: as already noted, the slope of the temperature time series changes at the same time as the destabilisation occurs (Fig. 5). The new slope is approximately equal to  $-2. \times 10^{-2} \text{ } ^\circ\text{C/year}$ , which multiplied by the ocean heat capacity (i.e.  $\rho c_p h$ ;  $\rho = 1000 \text{ kg/m}^3$ , the ocean density;  $c_p = 4000 \text{ J/kg/K}$ , the ocean thermal capacity per mass unit;  $h = 800 \text{ m}$ , the depth of the ocean in the model) gives about  $-2 \text{ W/m}^2$  over the ocean. When this value is distributed over the whole globe it gives  $-1.45 \text{ W/m}^2$  (the oceans constitute 70.5 % of the globe in the model), which is of the same order as the decrease of the net radiative flux at the TOA. Another view of the similarity between the energetics at the top of the atmosphere and in the ocean is given by Fig. 7. The evolution of the ocean heat budget weighted by the proportion of ocean grid-cells is compared to the evolution of the net radiative flux at the top of the atmosphere. The fluxes, represented as the departures from the respective means, are highly similar. This reinforces the picture of a destabilisation at the top of the atmosphere that is felt at the same time at the surface of the ocean.

## 4 The atmospheric component of the instability: detailed analysis

### 4.1 Method of decomposition

To understand the processes involved in the destabilisation of TRANSP<sup>+</sup>, we compare the state of the simulation before and after the year 6. The period before the destabilisation is designed as Period I, and the period after as Period II.



### 4.1.1 Analysis tool

The atmospheric radiative code of the coupled model is used as a diagnostic tool for off-line computations. It enables us to decompose the variations with time of the radiative fluxes into different contributions. The input parameters are cloudiness, specific humidity, air and surface temperatures, and surface albedo, all of which can contribute to the radiative flux variations. The outputs are the radiative fluxes at the TOA and at the surface. There is a 1 day-time step for the off-line computation and so the inputs are daily means. (The diurnal cycle is not considered in this version of the LMD AGCM.) The outputs are averaged over three years.

### 4.1.2 Principle of the decomposition

One assumes that a radiative flux  $F$  depends on  $n$  inputs  $(x_i)$  which are not necessarily independent. At each time step  $t$  (here in days),  $F$  can be written as a function of the inputs at this time,  $(x_i^t)$ :  $F = F(x_1^t, x_2^t, \dots, x_n^t)$ . We have 2 sets of time series  $(x_i^t), t \in \text{Period I}$  and  $(x_i^t), t \in \text{Period II}$ . The notation  $\bar{F}^I$  represents the average of  $F$  for  $t$  describing Period I.  $\bar{F}^I$  will also be written  $F(x_1^I, \dots, x_n^I)$ , which does not mean that we average the inputs, but that the time describes Period I. The same is true for  $F$  averaged over Period II,  $\bar{F}^{II}$ . The variation of  $F$  between these two periods is denoted by  $\Delta F = \bar{F}^{II} - \bar{F}^I$ .

We are interested in estimating how the variation of the input  $x_j$ , between Periods I and II, contributes variations in  $F$ . We estimate this contribution by processing the off-line computation of the radiative fluxes corresponding to the inputs  $(x_i^t), t \in \text{Period I}$ , except for variable  $x_j$  which is taken from Period II. The temporal mean of this new radiative flux is  $\bar{F}_j = F(x_1^I, \dots, x_j^{II}, \dots, x_n^I)$ . The difference  $(\Delta F)_j = \bar{F}_j - \bar{F}^I$  represents the variation of  $F$  associated with the direct effect of the variation of  $x_j$  when the other inputs are kept unchanged.

This method was first used by Wetherald and Manabe (1988), and has been applied at the LMD to investigate a variety of feedbacks in response to carbone dioxide increase (Le Treut et al. 1994).

### 4.1.3 Validity of the method

The fluxes  $F^I$  and  $F^{II}$  are slightly different from those computed by the coupled model because the time steps of the off-line (1 day) and the on-line (6 hours) computations are not the same. However the differences  $\Delta F$  are in very good agreement in the two computation methods, both for short wave radiation and longwave radiation at the TOA or at the surface (not shown here). Since we are mostly interested in differences  $(\Delta F)$  and  $(\Delta F)_j$ , our results indicate that the off-line computation is a useful tool for the decomposition of radiative fluxes.

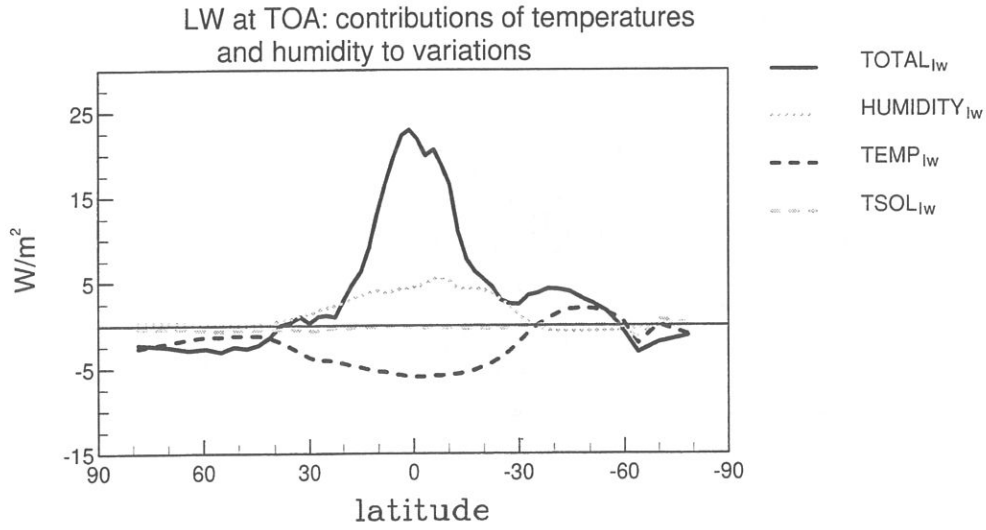


Figure 8: Zonal-mean temporal-mean variation (in  $\text{W/m}^2$ ) of the outgoing long-wave radiation at the top-of-the-atmosphere. Total variation (plain black curve) and contributions to this variation: contribution of air specific humidity (dotted grey curve), contribution of air and surface temperatures (dashed black curve), and contribution of surface-only temperatures (dashed grey curve). An increase of the emitted longwave radiation (cooling) is positive in sign. See text for the method of decomposition in contributions.

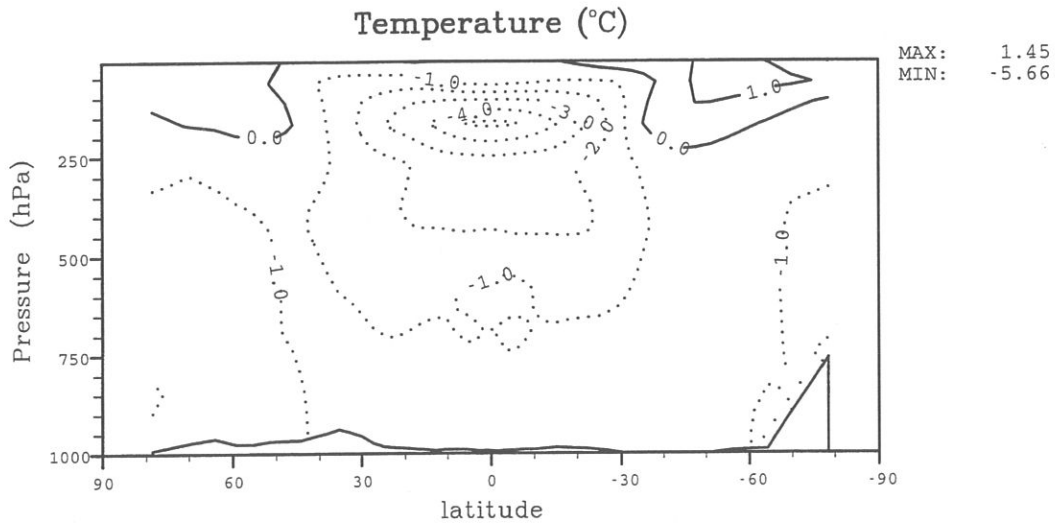


Figure 9: Difference (in  $^{\circ}\text{C}$ ) of the zonal-mean atmospheric temperature, between Period I and Period II (II minus I).

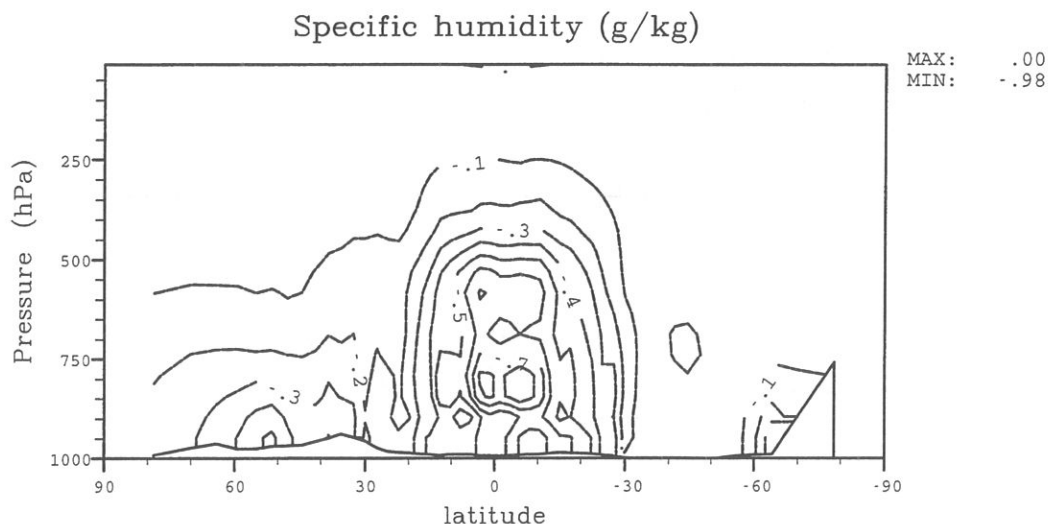


Figure 10: Difference (in g of water per kg of moist air) of the zonal-mean atmospheric specific humidity, between Period I and Period II.

## 4.2 Results

The method described in section 4.1 is applied to TRANSP<sup>+</sup>, for Period I (years 3, 4 and 5 of the simulation) and Period II (years 7, 8 and 9). The terms  $\Delta F$  and  $(\Delta F)_j$  (see section 4.1.2) are computed for the outgoing longwave radiation and the net short wave radiation at the TOA, and for the net longwave radiation and net short wave radiation at the surface.

### 4.2.1 Radiative fluxes at the top-of-the-atmosphere

*Contributions to longwave variations:*

Fig. 8 and Fig. 11 show  $\Delta F$  and  $(\Delta F)_j$  for the outgoing longwave radiation at the TOA in zonal and temporal average. In these figures the total variation of LW ( $\Delta F$ ) is given by the curve TOTAL<sub>lw</sub>. The sharp increase in the longwave emission already seen in Fig. 6 is located at low latitudes with an increase of more than 20 W/m<sup>2</sup> between the two periods around the equator.

The contribution of temperature is examined in Fig. 8. As shown by Fig. 9, as for the surface, the atmosphere cools at all altitudes except near the poles. The curve TEMP<sub>lw</sub> in Fig. 8 represents the contribution of air and surface temperature variations. This contribution is mostly negative and shows that in the absence of other feedbacks, the temperatures cooling would tend to reduce the longwave radiation emitted toward the space. By comparison, the surface-only temperature contribution (curve TSOL<sub>lw</sub>) is almost zero because the longwave emission at the TOA is practically insensitive to the surface longwave emission:

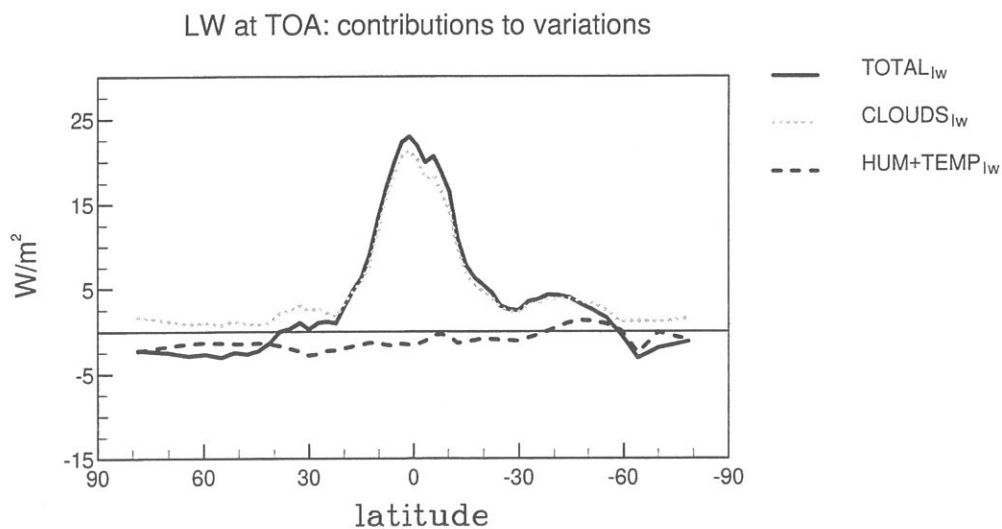


Figure 11: Same as Fig. 8, but with a different partitioning. Total variation of outgoing longwave radiation (plain black curve), and contributions to this variation: contribution of clouds (fraction and water content) (dotted grey curve), combined contribution of surface temperature, air temperature and air specific humidity (dashed black curve).

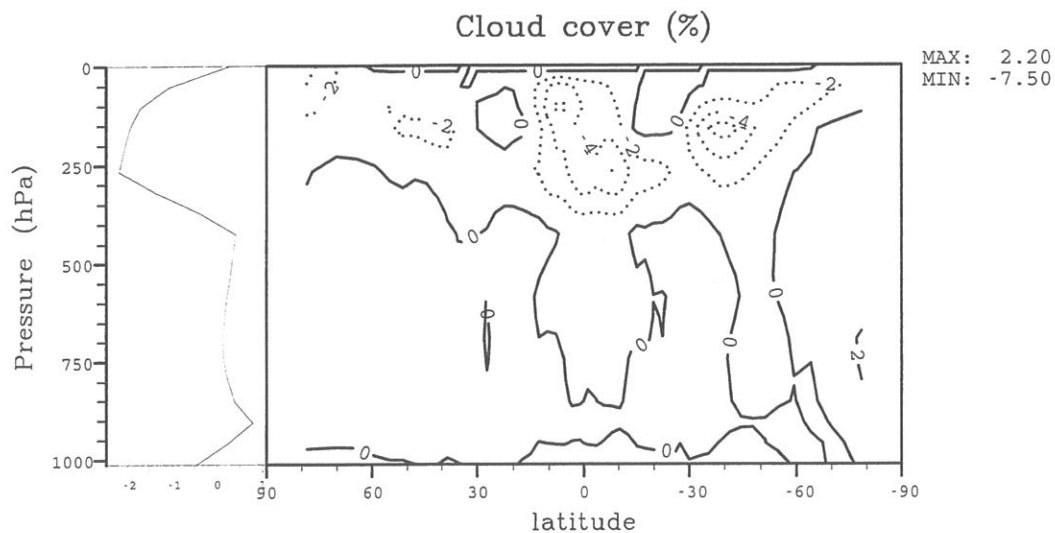


Figure 12: Difference (in percent of the model grid cell) of the zonal-mean cloud fraction, between Period I and Period II.

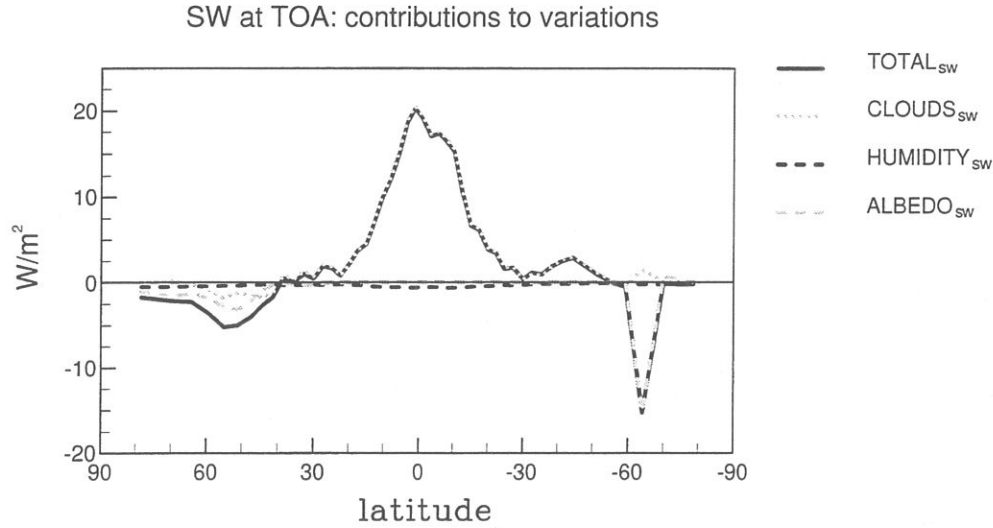


Figure 13: Same as Fig. 11, but for the net short wave radiation at the top-of-the-atmosphere. Total variation of short wave radiation (plain black curve) and contributions to this variation: contribution of clouds (dotted grey curve), contribution of air specific humidity (dashed black curve) and contribution of surface albedo (dashed grey curve). An increase of the incoming less reflected short wave radiation (warming) is positive in sign.

once emitted by the surface at its temperature, the longwave radiation is largely absorbed within the atmosphere and reemitted to the atmosphere own temperature. But Fig. 8 also shows that the temperatures effect is largely compensated by the specific humidity contribution (curve  $\text{HUMIDITY}_{lw}$ ). This positive contribution is due to the general decrease of specific humidity between the two periods (Fig. 10) which induces a decrease of the clear sky greenhouse effect which tends to increase the emission of longwave radiation at the TOA. Temperature and specific humidity contributions are very related (through the Clapeyron relationship) and have opposite signs, therefore we have computed in a single diagnostic their combined contribution. This combined contribution is represented by the curve  $\text{HUM} + \text{TEMP}_{lw}$  in Fig. 11. It is slightly negative and unable to explain the actual outgoing longwave radiation change.

The clouds contribution is represented by curve  $\text{CLOUDS}_{lw}$  in Fig. 11. It is very similar to the actual longwave radiation variation in the intertropical area ( $\text{TOTAL}_{lw}$ ). Therefore, the longwave variation is mainly explained by the evolution of cloudiness. The increase of the outgoing longwave radiation is due to a decrease of the high level clouds (cirrus clouds) between Period I and Period II (Fig. 12). The high level clouds are known to have a strong greenhouse effect at the top of the atmosphere because when they absorb the atmospheric longwave radiation, they reemit it toward space at the temperature of their top, which



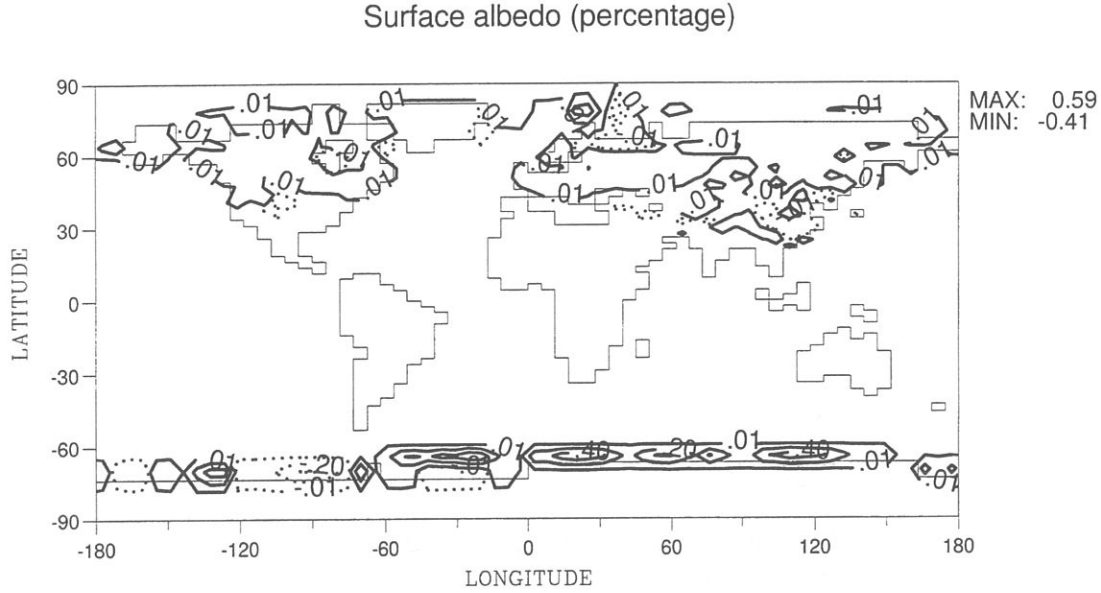


Figure 14: Difference (in %) of surface albedo (average of day-by-day albedo), between Period I and Period II.

is low. Therefore, when they decrease, a larger amount of longwave radiation is emitted toward space at the TOA. In addition, the decrease of the high level absorption also explains the stronger cooling of the high atmosphere of the model at low latitudes (Fig. 9).

#### *Contributions to short wave variations:*

Total variation of net short wave radiation at the TOA and contributions of clouds, specific humidity and surface albedo, are shown in Fig. 13. As for the longwave, the increase of short wave radiation (Fig. 6) occurs in the intertropical area (curve  $TOTAL_{sw}$  in Fig. 13). It is also explained by the decrease of high level cirrus clouds which lowers the planetary albedo (curve  $CLOUDS_{sw}$ ).

In addition, in southern high latitudes, there is a sharp contribution of the surface albedo shown by curve  $ALBEDO_{sw}$  in Fig. 13 ( $-15 \text{ W/m}^2$  at  $65\text{S}$ ). It is due to an extension of the sea ice cover between the two periods (Fig. 14).

The specific humidity contribution ( $HUMIDITY_{sw}$  in Fig. 13) is a slight one, mainly explained by the fact that a lower water vapor content decreases the amount of short wave energy absorbed in the atmosphere: a part is absorbed at the surface instead (see Fig. 16), and the other part is reflected toward space (shown by curve  $HUMIDITY_{sw}$ ).

The temperatures contribute to the coefficients for the absorption by ozone of the ultraviolet and near infrared range radiations, but since it is very low, it is not shown here.

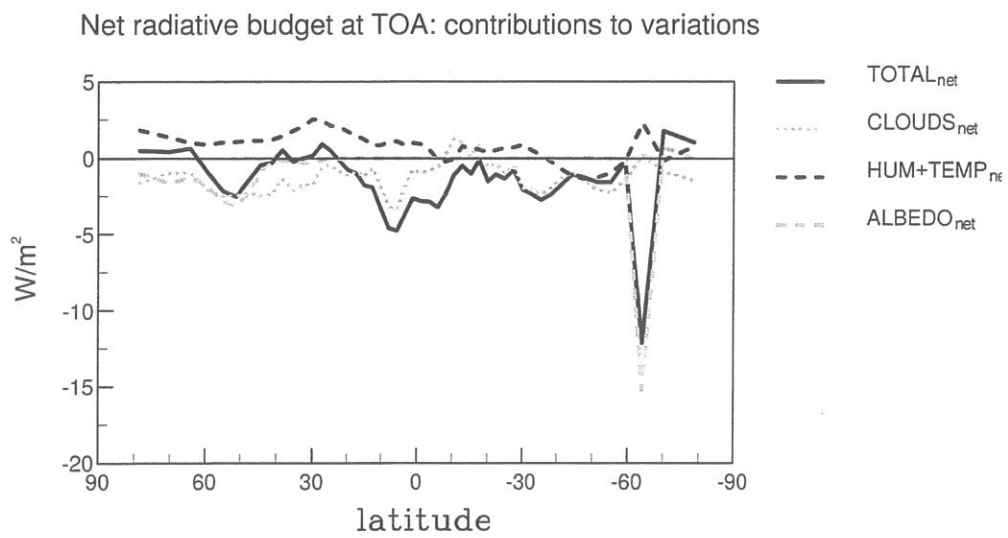


Figure 15: Same as Fig.13, but for the net radiative budget at the top-of-the-atmosphere (difference between net short wave radiation and outgoing longwave radiation). Total variation of the net radiative budget (plain black curve) and contributions to this variation: contribution of clouds (dotted grey curve), combined contribution of surface temperature, air temperature and air specific humidity (dashed black curve), and contribution of surface albedo (dashed grey curve). An increase of the incoming net radiative budget (warming) is positive in sign.

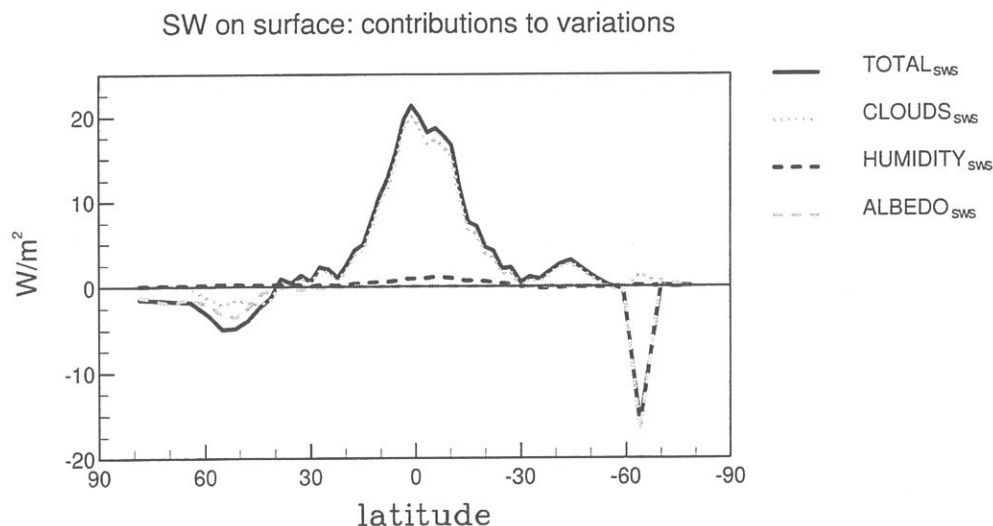


Figure 16: Zonal-mean temporal-mean variation (in  $\text{W/m}^2$ ) of the net short wave radiative flux at the surface. Total variation (plain black curve) and contributions to this variation: contribution of clouds (dotted grey curve), contribution of air specific humidity (dashed black curve), contribution of surface albedo (dashed grey curve). An increase of the absorbed short wave radiation (warming) is positive in sign.

*Contributions to variations of the net radiative budget at the TOA:*

Fig. 15 shows the variation of the net radiative budget at the TOA and the contributions of clouds, albedo and combination of air specific humidity and air and surface temperatures. Since the contributions of the longwave and shortwave fluxes on the global system energetics are of opposite signs, the resulting contributions to the net radiative budget have lower values. It is negative in most areas with local maxima at the equator (effect of clouds, curve  $\text{CLOUDS}_{net}$ ) and at 65S (effect of sea ice, curve  $\text{ALBEDO}_{net}$ ).

Note, that contributions  $\text{HUM} + \text{TEMP}_{net}$  and  $\text{CLOUDS}_{net}$  do not sum well to give the actual variation at low latitudes because water vapor greenhouse effect, cloud radiative forcing and vertical temperature profile have very interdependent and complex impacts on the longwave component.

#### 4.2.2 Radiative fluxes at the surface

At the surface, the energy budget is more complex than at the TOA because of the additional contributions of the turbulent heat fluxes.

*Contributions to short wave variations:*

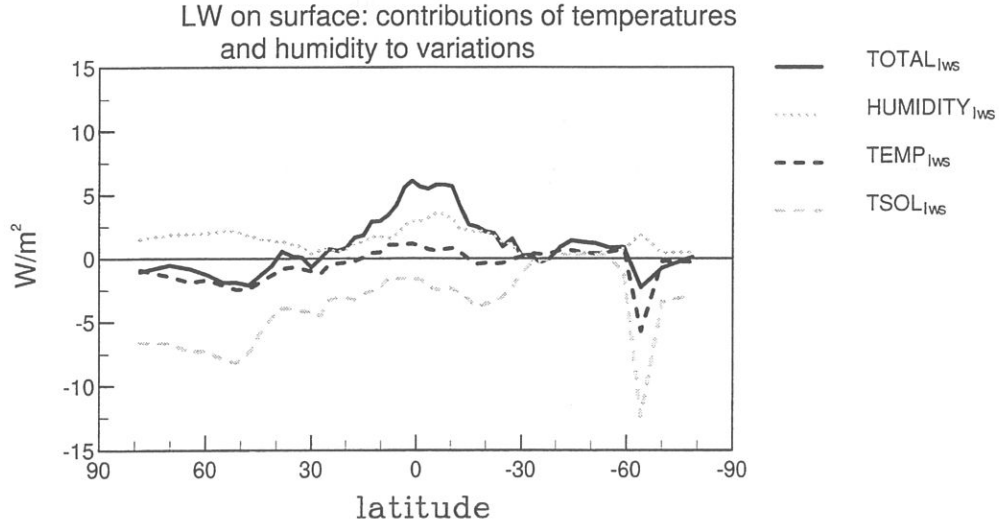


Figure 17: Same as Fig. 16 but for the net longwave radiative flux at the surface. Total variation (plain black curve) and contributions to this variation: contribution of air specific humidity (dotted grey curve), contribution of air and surface temperatures (dashed black curve), contribution of surface only temperatures (dashed grey curve). An increase of the outgoing longwave radiation (cooling) is positive in sign.

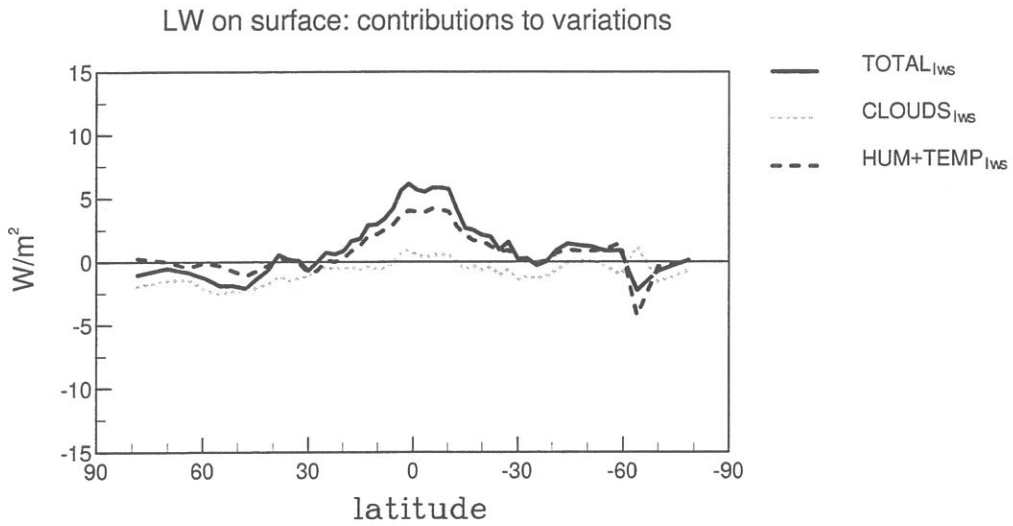


Figure 18: Same as Fig. 17 but with a different partitioning. Total variation of the surface net longwave radiative flux (plain black curve), contribution of clouds (dotted grey curve) and combined contribution of air temperature, surface temperature and air specific humidity (dashed black curve). An increase of the outgoing longwave radiation (cooling) is positive in sign.

Net radiative budget at the surface: contributions to variations

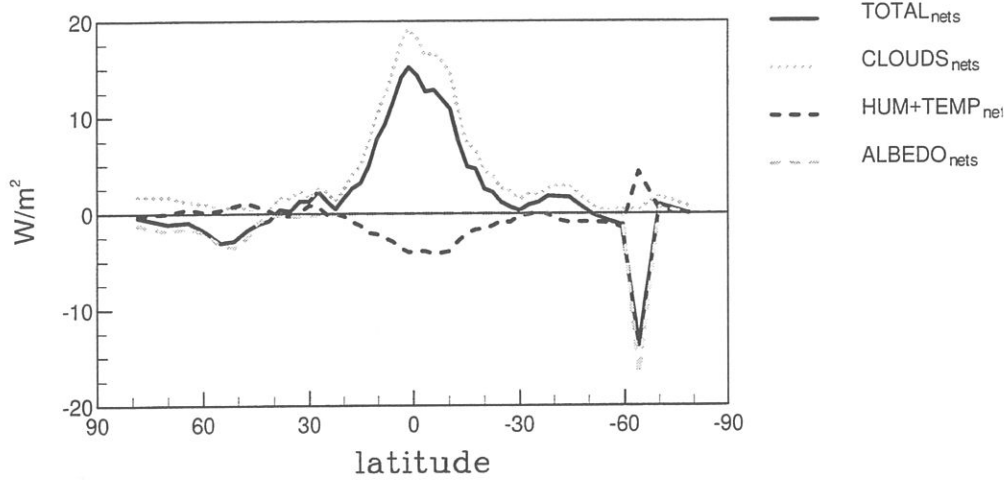


Figure 19: Same as Fig. 18 but for the net surface radiative budget. Total variation (plain black curve) and contributions to this variation: contribution of clouds (dotted grey curve), combined contribution of air temperature, surface temperature and air specific humidity (dashed black curve), contribution of surface albedo (dashed grey curve). An increase of the incoming radiative flux (warming) is positive in sign.

The difference of net short wave radiation between the top of the atmosphere and the surface is only due to the absorption of short wave energy by the atmosphere. Since this absorption varies only slightly, the short wave radiation characteristics at the surface (Fig. 16) are very similar to those at the TOA (Fig. 13). The only qualitative difference is the air specific humidity contribution (curve  $\text{HUMIDITY}_{lws}$  in Fig. 16) which has the opposite sign: because of less absorption by the water vapor, a larger part of short wave energy is absorbed by the surface (already mentioned in section 4.2.1).

#### *Contributions to longwave variations:*

The longwave radiation at the surface is the difference of the surface emission and the atmosphere emission toward the surface. Its variations are therefore qualitatively different from the top of the atmosphere. The total variation of the surface longwave radiation is lower than it was at the TOA: the curve  $\text{TOTAL}_{lws}$  in Fig. 17 shows that the maximum increase of the surface longwave radiation reaches a value of  $5 \text{ W/m}^2$  in the intertropical area when it was more than  $20 \text{ W/m}^2$  at the TOA. By contrast with the TOA, the surface cooling is efficient in reducing the emitted longwave radiation (curve  $\text{TSOL}_{lws}$ ). But the air cooling contributes to reduce the downwelling longwave radiation and compensates for

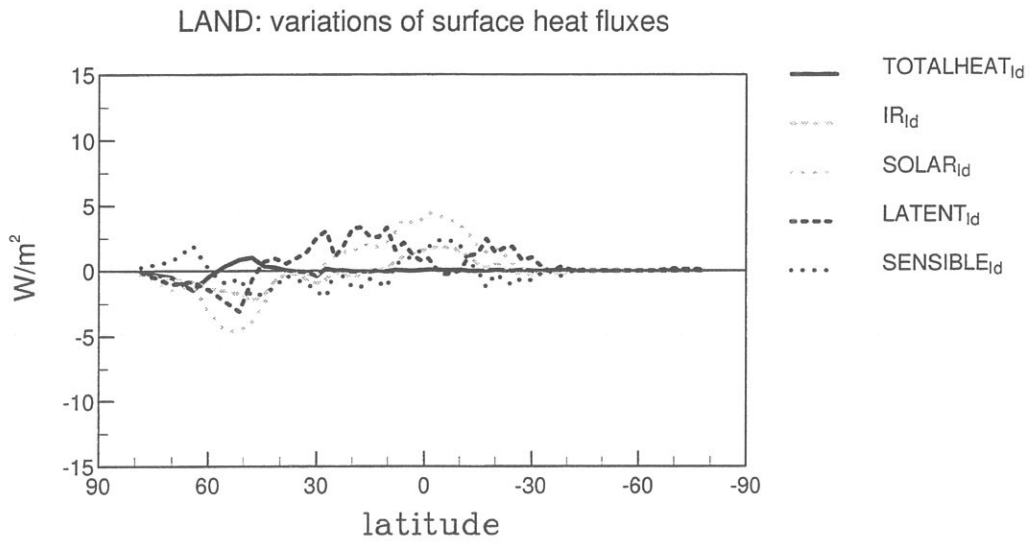


Figure 20: Difference over land (in  $W/m^2$ ) of zonal-mean annual-mean surface heat fluxes, between Period I and Period II (II minus I): total heat budget (plain black curve), longwave radiation (dashed grey curve), short wave radiation (dotted grey curve), latent heat flux (dashed black curve) and sensible heat flux (dotted black curve). Increase of incoming short wave radiation and incoming total heat flux (warming) are positive in sign. Longwave, latent and sensible heat fluxes follow the opposite convention. (The values are weighted by the rate of land for each latitudinal band so that the sum of these curves and those of Fig. 21 gives the actual zonal mean.)

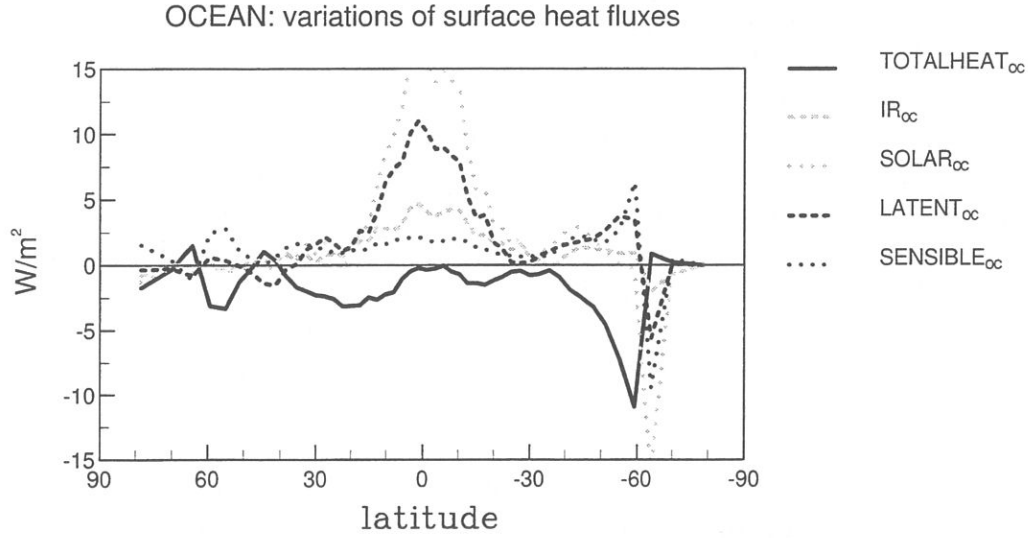


Figure 21: Same as Fig. 20 but over the oceans.

the surface contribution: the curve  $TEMP_{lws}$  is therefore close to zero. On the other hand, the reduction of specific humidity in the lower atmosphere induces a lower clear-sky greenhouse effect at the surface (decrease of downwelling long-wave radiation) and therefore a cooling of the surface (curve  $HUMIDITY_{lws}$  above zero). Fig. 18 shows that the combined contribution of temperatures and specific humidity (curve  $HUM+TEMP_{lws}$ ) explains, to a large extent, the total variation of the longwave radiation at the surface, whereas the contribution of clouds (curve  $CLOUDS_{lws}$ ) is low because the high level clouds have only a small impact on the surface greenhouse effect.

*Contributions to variations of the surface net radiative budget:*

The effects of clouds (warming through SW), surface albedo (cooling through SW) and the combination of specific humidity and temperatures (cooling through LW) combine to give the variation of the net radiative budget (Fig. 19). Again, the cloud contribution is the strongest and induces a warming by contrast with the top-of-the-atmosphere.

#### 4.2.3 Surface heat budget

In section 4.2.2, we have seen that the evolution of the radiative budget at the surface is positive in sign in the equatorial region. Indeed, the decrease of the surface heat budget occurs through the turbulent heat fluxes variations (in addition to the longwave radiative flux). Over land, the surface heat budget changes only slightly between Period I and Period II (Fig. 20). Though the absorbed short wave radiation increases in the intertropical area (curve  $SOLAR_{ld}$ ), it is compensated, near the equator by longwave radiation (curve  $IR_{ld}$ ) and sensible



heat flux (curve  $\text{SENSIBLE}_{ld}$ ) and, near the tropics, by the latent heat flux (curve  $\text{LATENT}_{ld}$ ). Because of the low thermal capacity of the land surface in the model, the surface heat budget is almost balanced at every time and a variation of one flux is compensated by variations of the other.

The situation is different over the oceans: differences between Periods I and II for surface heat budget and short wave, longwave, latent and sensible heat fluxes are shown in Fig. 21. In the intertropical area, as already seen, the increase of absorbed short wave radiation is the largest variation. In the equatorial area (5S-5N) it is balanced by increases of the latent, longwave and sensible heat fluxes (respectively  $10 \text{ W/m}^2$ ,  $5 \text{ W/m}^2$  and  $2 \text{ W/m}^2$ ). In most other regions, the surface heat budget decreases, with generally a higher contribution of the latent heat flux.

Therefore, all non-solar heat fluxes contribute to the transmission of the energetic destabilisation, from the top of the atmosphere to the surface.

## 5 Discussion and conclusion

The variability displayed by the coupled ocean-atmosphere models may have a large variety of causes, some of them external, some of them internal to the climate system. The model presented in this paper, as it uses prescribed oceanic heat transport, can be used to test the sensitivity of the climate system to small variations of this oceanic heat transport.

Previous studies with the same model (Cohen-Solal and Le Treut 1997) had shown that in some cases the coupled system was able to compensate a loss of oceanic energy transport by an increased atmospheric energy transport.

In the present article, we have presented a set of experiments where the ocean energy transport has been modified in the tropical region. In one of these experiments we find a very intense response of the coupled system. It is due to an instability mechanism which we have studied in detail.

In this simulation the surface becomes cooler, the specific humidity in the low atmosphere and the temperature of the high atmosphere decrease. The evolution of the model is triggered (at least partially) by an atmospheric feedback mechanism which involves the decrease of high level clouds in the intertropical region. As these clouds have a strong greenhouse effect, their decrease induces an increase of the outgoing longwave radiation. This loss of heat is only partially balanced by the decrease of the planetary albedo resulting from the lesser cloudiness. Therefore there is a loss of energy by the global system at the top of the atmosphere and a cold drift.

The decrease of these cirrus clouds in the model may have different causes. The energy by decrease of the surface specific humidity and hence of water vapor transported at higher atmospheric levels can be one of these causes. Variations of atmospheric circulation or convective processes in the tropical region can also

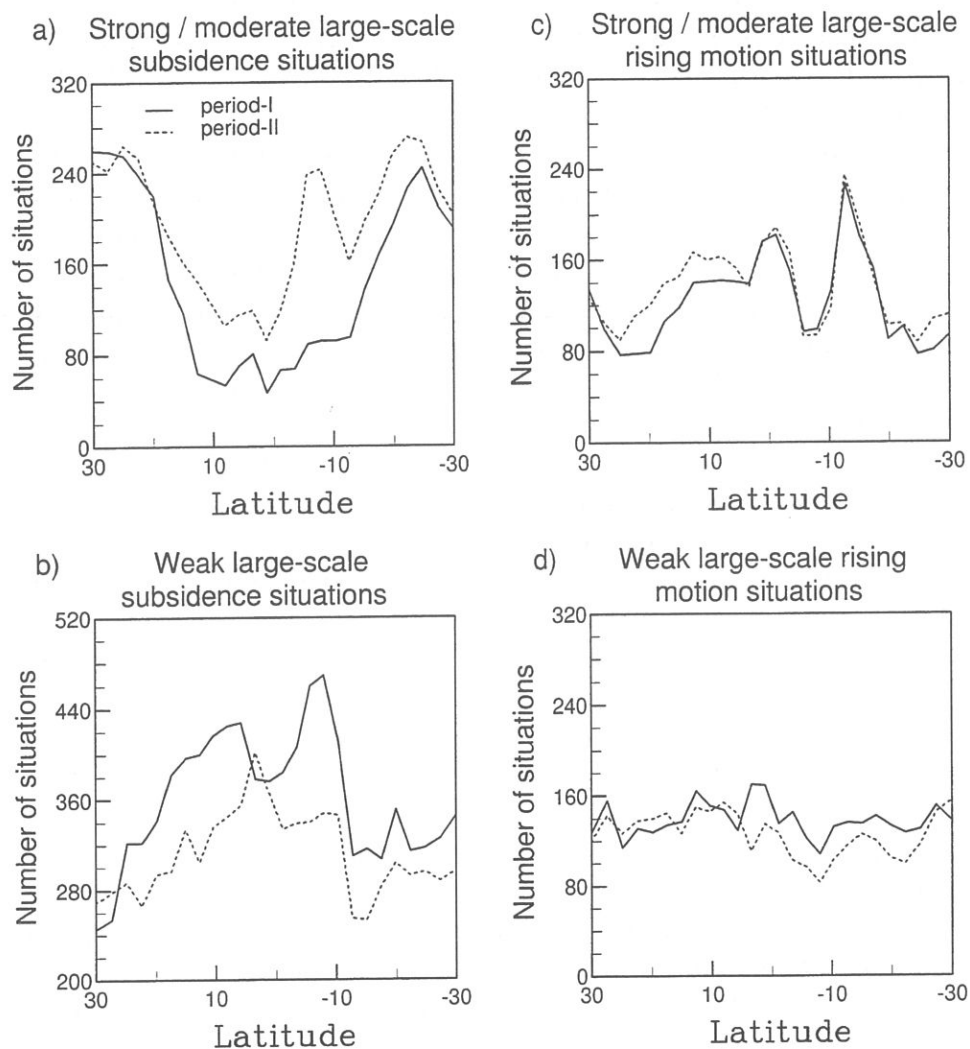


Figure 22: Occurrence (expressed as the number of points within each latitudinal band of the model) of the 4 regimes of vertical motion defined in the text. Calculation made with the simulated vertical velocity  $dp/dt$  at 500hPa, in monthly means (average over 3 years) for period I (plain line) and period II (dotted line).

contribute to the high-level cloud decrease. The convection is affected both by specific humidity and temperature variations at the surface and in altitude: they have here opposite contributions on the convection which indeed does not change significantly (not shown here).

By contrast, the Hadley circulation is changed by the cooling. We have examined the simulated vertical velocity ( $dp/dt$ , where  $p$  is the pressure and  $t$  the time) at 500hPa in the 30S-30N latitudinal band. The vertical motion situations have been classified in 4 regimes: strong/moderate subsidence ( $dp/dt > 20\text{hPa/day}$ ), weak subsidence ( $20 > dp/dt > 0$ ), weak rising motion ( $0 > dp/dt > -20$ ) and strong/moderate rising motion ( $-20\text{ hPa/day} > dp/dt$ ) (Bony et al. 1997). The comparison of situations before and after the destabilisation shows that there is an increase of the number of situations of strong/moderate subsidence and a decrease of the number of weak subsidence situations (Fig. 22 a and b). The situations of strong/moderate rising motion increase also but slightly (Fig. 22 c) while the weak vertical rising motions situations become less frequent in the tropical area (Fig. 22 d). This intensification of the descending movements is consistent with the clouds decrease in altitude.

A question that arises from this study is whether our model's feedback relating clouds and sea surface temperatures is realistic. Bony et al. (1997) have studied the relationship between cloud radiative forcing and sea surface temperature in the tropical region and the influences of the large-scale circulation. By studying interannual variations in observational datasets of the tropical region, they show that the cloud radiative forcing at the top of the atmosphere increases with the sea surface temperature because of cloudiness increase and an enhanced radiative forcing in the longwave. According to the authors, a warming of 1K of the surface ocean in areas where it is originally comprised between 25-27K induces an increase of the cloud cover by ca. 2 percent. This increase is mostly due to changes in the mean vertical circulation. They also find that the cloud radiative forcing increases by  $6.7\text{ W/m}^2/\text{K}$  in the shortwave (cooling) and  $9.2\text{ W/m}^2/\text{K}$  in the longwave (warming) for the same oceanic tropical areas with a net forcing corresponding to an enhancement of the warming by clouds ( $2.5\text{ W/m}^2/\text{K}$ ). This stronger effect of clouds in the infrared spectrum is consistent with the positive feedback of clouds in our model.

Therefore, the oscillations of the ocean energy transport from one year to the other, may bring important climate variations in coupled models or in the reality. Our results must however be ascertained by a careful validation of the climate of the model, in general, and the cloud schemes, in particular. Also, we think that our findings may not be generalized too quickly to explain other models' long term drifts since only a single model is studied here.

## 6 Acknowledgements

The authors are grateful to Ben Santer for his careful reading of the manuscript and his valuable comments. ECS expresses her thanks to Larry Gates and the PCMDI staff for the exceptional conditions of work and the support she has received in 1996-1997. This work was performed under the auspices of the CNRS (Centre National pour la Recherche Scientifique, France) and the U.S. Department of Energy, Environmental Sciences Division, at Lawrence Livermore National Laboratory (Livermore, USA) under contract W-7405-ENG-48. The simulations were carried out at the IDRIS (Institut du Développement et des Ressources en Informatique Scientifique, Orsay, France) on a Cray 98.

## References

- Alexander R, Mobley R (1976) Monthly average sea surface temperatures and ice-pack limits on a  $1^\circ$  global grid. *Month W Rev* 104: 143-148.
- Bony S, Lau K-M, Sud Y C (1997) Sea surface temperature and large-scale circulation influences on tropical greenhouse effect and cloud radiative forcing. *J Climate* 10: 2055-2077.
- Boville B A, Cent P R, Kiehl J T, Large W G (1997) Century simulations with the NCAR Climate System Model. *Science*, submitted.
- Braconnot P, Marti O, Joussaume S (1997) Adjustment and feedbacks in a global coupled ocean-atmosphere model. *Clim Dyn* 13: 507-519.
- Cohen-Solal E, Le Treut H (1996) Impact of ocean optical properties on seasonal SST: results with a surface ocean model coupled to the LMD AGCM. *Clim Dyn* 12: 417-433.
- Cohen-Solal E, Le Treut H (1997) Role of the ocean heat transport on climate dynamics: A sensitivity study with an atmospheric general circulation model. *Tellus* 49A: 371-387.
- Covey C, Santer B D, Cohen-Solal E (1996) CMIP: A study of climate models and natural climate variability, in *Proceedings of the Workshop on Dynamics and Statistics of Secular Climate Variations*, Miramare-Trieste, Italy, 4-8 December 1995, J. L. Kinter III and E. K. Schneider, eds., Report No. 26, Center for Ocean-Land-Atmosphere Studies, pp 11-15.
- Fouquart Y, Bonnel B (1980) Computations of solar heating of the earth's atmosphere: A new parametrisation. *Beiträge zur Physik der Atmosphäre* 53: 35-62.
- Gaspar P (1988) Modeling the seasonal cycle of the upper ocean. *J Phys Ocean* 18: 161-180.
- Gleckler P J, Randall D A, Boer G, Colman R, Dix M, Galin V, Helfand M, Kiehl J, Kitoh A, Lau W, Liang X-Z, Lykossov V, McAvaney B, Miyakoda K, Planton S, Stern W (1995) Cloud-radiative effects on implied oceanic energy transports as simulated by atmospheric general circulation models. *Geoph Research Letters* 22(7): 791-794.
- Gleckler P J, Weare B C (1997) Uncertainties in global ocean surface heat flux climatologies derived from ship observations. *J Clim*, In press.

Hasselmann K (1988) Some problems in the numerical simulation of climate variability using high resolution coupled models. in (M E Schlesinger ed.) *Physically based modelling and simulation of climate and climatic change*, Part I, Kluwer Academic Publishers, pp 583–614.

Hibler III W (1979) A dynamic thermodynamic sea ice model. *J Phys Ocean* 9: 815–846.

Kuo H L (1965) On formation and intensification of tropical cyclones through latent heat release by cumulus convection. *J Atmos Sc* 22: 1482–1497.

Le Treut H, and Li Z X (1991) Sensitivity of an atmospheric general circulation model to prescribed SST changes: Feedback effect associated with the simulation of cloud optical properties. *Clim Dyn* 5: 175–187.

Le Treut H, Li Z X, Forichon M (1994) Sensitivity of the LMD general circulation model to greenhouse forcing: Analysis of the atmospheric feedback effects. *J Climate* 7(12): 1827–1841.

Levitus S (1982) *Climatological atlas of the world ocean*, Professional Paper 13, NOAA ; U.S. Department of Commerce, Washington.

Morcrette J-J (1991) Radiation and cloud radiative properties in the European Centre for Medium Range Weather Forecasts forecasting system. *J Geoph Res* 96: 9121–9132.

Rahmstorf S (1995) Climate drift in an ocean model coupled to a simplified perfectly matched atmosphere. *Clim Dyn* 11: 447–458.

Sadourny R, Laval K (1984) January and July performance of the LMD general circulation model, in *New Perspectives in Climate Modelling*, edited by A. Berger and C. Nicolis, number 16 in Elsevier Sc., pp 173–197.

Sausen R, Barthel K, Hasselmann K (1988) Coupled Ocean-Atmosphere Models with flux correction. *Clim Dyn* 2: 145–163.

Semtner A (1976) A model for the thermodynamic growth of sea ice in numerical investigations of climate. *J Phys Ocean* 6: 379–389.

Weaver A J, Hughes T M C (1996) On the incompatibility of ocean and atmosphere models and the need for flux adjustments. *Clim Dyn* 12: 141–170.

Wetherald R T, Manabe S (1988) Cloud feedback processes in a general circulation model. *J Atmos Sc* 45: 1397-1415.



## Déjà paru :

- 1 : **Janvier 1998** Agnès Ducharne, Katia Laval and Jan Polcher,  
*Sensitivity of the hydrological cycle to the parameterization of soil hydrology in a GCM*
- 2 : **Janvier 1998** Marina Lévy, Laurent Mémerly and Jean-Michel André ,  
*Simulation of primary production and export fluxes in the Northwestern Mediterranean Sea*
- 3 : **Février 1998** Valérie Masson, Sylvie Joussaume, Sophie Pinot and Gilles Ramstein, *Impact of parameterizations on simulated winter mid-Holocene and Last Glacial Maximum climatic changes in the Northern Hemisphere*
- 4 : **Mars 1998** Jérôme Vialard et Pascale Delecluse, *An OGCM Study for the TOGA Decade. Part I: Role of Salinity in the Physics of the Western Pacific Fresh Pool, Part II: Barrier layer formation and variability*
- 5 : **Avril 1998** O. Aumont, J. C. Orr, P. Monfray, and G. Madec, *Nutrient trapping in the equatorial Pacific: The ocean circulation solution*

